

Impact response of steel-concrete composite panels: Experiments and FE analyses

Weiye Zhao^a, Quanquan Guo^{*}, Xuqiang Dou^b, Yao Zhou^c and Yinghua Ye^d

School of Transportation Science and Engineering, Beihang University, Beijing 100191, China

(Received July 3, 2017, Revised October 7, 2017, Accepted October 8, 2017)

Abstract. A steel-concrete composite (SC) panel typically consists of two steel faceplates and a plain concrete core. This paper investigated the impact response of SC panels through drop hammer tests and numerical simulations. The influence of the drop height, faceplate thickness, and axial compressive preload was studied. Experimental results showed that the deformation of SC panels under impact consists of local indentation and overall bending. The resistance of the panel significantly decreased after the local failure occurred. A three-dimensional finite element model was established to simulate the response of SC panels under low-velocity impact, in which the axial preload could be considered reasonably. The predicted displacements and impact force were in good agreement with the experimental results. Based on the validated model, a parametric study was conducted to further discuss the effect of the axial compressive preload.

Keywords: steel-concrete composite panel; low-velocity impact; axial preload; dynamic response; numerical simulation

1. Introduction

The design of steel-concrete composite (SC) structures is typically governed by the ultimate limit state performance under static loading or seismic action. Based on the investigations on the behavior of SC structural members during the past four decades, design specifications were developed in many countries (e.g., JEAC 4618-2009 (2009), KEPIC-SNG (2010), and ANSI/AISC N690s1-15 (2015)). Some SC structures must be designed for impact loads, such as shear walls of high-rise buildings, containment shells of nuclear facilities, slabs or walls in protective structures, etc. However, the response of SC members under impact is an area of research that is still not well understood.

To date, the majority of the related research was focused on the localized damage, especially for SC slab or wall elements. The work can be traced to the 1940s when the integrity of reinforced concrete (RC) structures under kinetic energy weapons was the most concerned issue after the Second World War. Empirical formulae for calculating penetration, scabbing, and perforation were developed (Kennedy 1975, Sliter 1980, Grisaro and Dancygier 2014). An effective approach to enhance the impact resistance of RC barriers is to attach steel liners to the surface by means of epoxy adhesives or stud connectors. Experimental studies showed that the steel plate on the rear face could effectively

prevent the scabbed concrete debris from flying into the structures (Walter and Wolde-Tinsae 1984, Barr 1990, Tsubota *et al.* 1993, Grisaro and Dancygier 2015). SC panels are proved to have good impact resistance due to the structural similarity to the reinforced concrete panels with steel liners (Hashimoto *et al.* 2005, Mizuno *et al.* 2005, Sadiq *et al.* 2014, Lee and Kim 2016).

However, limited works have been done on the dynamic response of SC panels subjected to low-velocity impact. Remennikov *et al.* (2012, 2013) conducted experimental investigations on axially restrained non-composite SC panels. The panels underwent large deformation and tensile membrane resistance was developed due to the boundary constraints. The panels exhibited good ability in energy dissipation. Drop hammer tests were carried out on SC beams and slabs with innovative J-hook connectors (Liew *et al.* 2009, Sohel and Liew 2014). This type of connection could effectively prevent the separation of the faceplates. Based on the principle of energy conservation, theoretical models were proposed to analyze the impact response of SC beams and slabs. Bruhl *et al.* (2015a, b) investigated the global deformation of SC panels by finite element analyses. The static bearing mechanism was employed in single-degree-of-freedom and two-degree-of-freedom mass-spring models to predict the deformation of SC panels.

In practical applications, dead and live compressive loads are dominant during service for the SC panels used as shear walls. The bearing characteristic and stress distribution may be changed under the influence of the axial compression. However, no study so far has studied the performance of SC panels subjected to axial compression and impact loading. This paper presents experimental and numerical investigations on the effect of axial compression prior to impact. A critical axial compression ratio is suggested for anti-impact design.

*Corresponding author, Ph.D., Associate Professor,

E-mail: qq_guo@buaa.edu.cn

^a Ph.D. student

^b Graduate Student

^c Ph.D., Associate professor

^d Ph.D., Professor

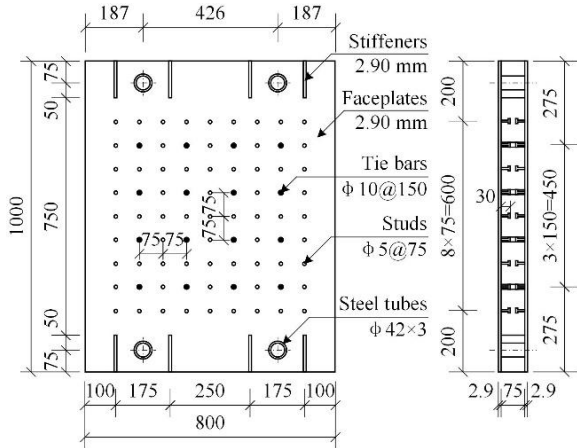


Fig. 1 A typical drawing of the specimen (Series T03)

2. Experimental program

2.1 Specimen preparation and material properties

Ten rectangular SC panel specimens were designed in this experiment, as shown in Fig. 1. The dimension of all specimens was 1000 mm × 800 mm. The thickness of the concrete core (t_c) was 75 mm. Steel faceplates with three different thicknesses (t_s) were used for specimen series T03, T04, and T05. Headed stud bolts measuring 5 mm × 30 mm (diameter × length) were welded on the inner surface of the steel faceplates. Tie bars with 10 mm diameter were also used to connect both faceplates. The spacing of the tie bars and the studs were 150 mm and 75 mm, respectively.

To keep the thin faceplates free of deformation caused by thermal stress, stiffening ribs were spot-welded on the outer surface before welding the connectors. Since the spacing between the two faceplates was small, the tie bars were plug-welded through punching holes on the faceplates. After the steel module cooled, the stiffeners were cut off. It was found that the evenness of the specimen could be well guaranteed.

Four circular openings allowing anchor bolts to pass through were fabricated and stiffening steel tubes and ribs were arranged near the openings. The diameter of the openings was large enough so that the specimen could deform freely under the action of axial compression and impact loading.

Tensile coupon tests were conducted to obtain the

Table 1 Steel material properties

Part	t_s /mm	d /mm	f_y /MPa	f_u /MPa	E_s /GPa	ϵ_{ult}
Steel plates	2.90	-	287	437	208	0.306
	3.80	-	658	719	206	0.319
	5.35	-	275	408	208	0.326
Tie bars	-	10.00	338	486	206	0.324
Studs	-	4.24*	320	400	206	-

* Effective diameter of M5 bolt

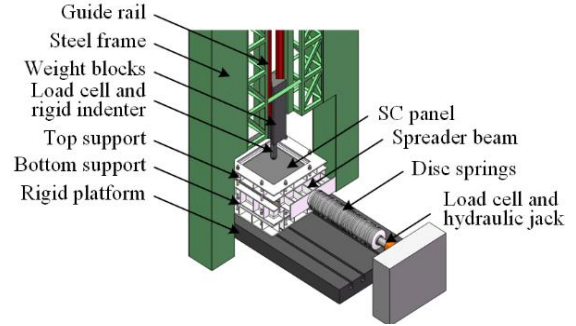


Fig. 2 The drop hammer impact test set-up

mechanical properties of the steel plates and the tie bars. Table 1 shows the measured thickness (t_s) or diameter (d), yield stress (f_y), ultimate strength (f_u), elastic modulus (E_s) and ultimate strain (ϵ_{ult}) of the steel materials. For the studs, the nominal parameters of property class 4.8 hexagon head bolt are used as the reference. Self-consolidating concrete was used as the core. Standard prismatic specimens were tested at 28 days after casting. The average density (ρ_c), unconfined compressive strength (f_c), and elastic modulus (E_c) were 2300 kg/m³, 48.7 MPa, and 3.05 × 10⁴ MPa, respectively.

2.2 Test set-up and data measurements

The drop hammer impact test rig used to complete the experiment is shown in Fig. 2. From the top of the steel frame to the rigid platform, a drop height (H) of up to 12.6 m is available. The falling of the drop hammer is frictionless, because the clearance between the drop hammer and the guide rails is large enough. The impact velocity (V_0) can be calculated by the free fall formula (i.e., $V_0^2 = 2gH$, where $g = 9.797$ m/s² is the local acceleration of gravity). The drop hammer consists a set of weight blocks, an 80-mm diameter rigid hemispherical indenter, and a 1000-kN capacity load cell installed between the weight blocks and the indenter. The total mass of the drop hammer (m) was 233.5 kg and different impact energies (E_0) were achieved by releasing the hammer at different heights (i.e., $E_0 = mgh$). The SC panel specimen was clamped between two support frames with 20 mm diameter rollers. The support system and the specimen were fixed to the rigid platform by eight high strength M24 bolts. The spans in both lengthwise and widthwise directions were 750 mm.

The detailed information of the specimens is illustrated in Table 2, where the letter “T” and the flowing number in the name of the specimen denote the thickness of the steel faceplates, the letter “H” and the following number denote the drop height. For Series T03, the drop hammer was released from five different heights: 1.5 m, 3.0 m, 4.5 m, 6.0 m, and 7.5 m; while for Series T04 and T05, the drop height was 4.5 m. The letter “N” represents the axial preload condition. For the panels impacted with the lowest, the medium and the highest energy levels in Series T03, an axial compressive load (N) in the lengthwise direction was applied prior to impact by a hydraulic jack. A load cell used to monitor the axial preload was attached to the jack. To keep the axial preload relatively stable, a set of disc springs



Fig. 3 Measuring points at the bottom steel faceplate

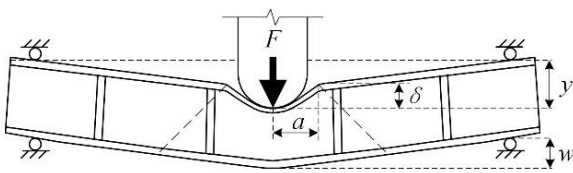


Fig. 4 Deformation of SC panel under impact

was positioned between the spreader beam and the load cell to reduce fluctuation during impact (Wang *et al.* 2013).

The detailed information of the specimens is illustrated in Table 2, where the letter “T” and the flowing number in the name of the specimen denote the thickness of the steel faceplates, the letter “H” and the following number denote the drop height. For Series T03, the drop hammer was released from five different heights: 1.5 m, 3.0 m, 4.5 m, 6.0 m, and 7.5 m; while for Series T04 and T05, the drop height was 4.5 m. The letter “N” represents the axial preload condition. For the panels impacted with the lowest, the medium and the highest energy levels in Series T03, an axial compressive load (N) in the lengthwise direction was applied prior to impact by a hydraulic jack. A load cell used to monitor the axial preload was attached to the jack. To keep the axial preload relatively stable, a set of disc springs was positioned between the spreader beam and the load cell to reduce fluctuation during impact (Wang *et al.* 2013).

During impact, the motion of the drop hammer was captured by a high-speed camera at a frame rate of 2000 fps. Seven potentiometric displacement transducers were used to measure the displacement histories of the bottom face, as shown in Fig. 3. The drawbars of the transducers were attached to the steel faceplate by bolted connections so that the rebound of the specimen could be fully recorded. A National Instruments (NI) data acquisition system equipped with two PXIe-4331 modules was used to record the experimental data at a rate of 100 kHz.

3. Experimental results

3.1 Damage description

All specimens exhibited a deformation combined by local indentation and overall bending, as shown in Fig. 4. The central deflection (w) of the panel was measured by the potentiometric displacement transducer W1 (Fig. 3). The displacement of the drop hammer is designated as y , whilst δ and a refers to the depth and radius of the indentation zone.

Fig. 5 shows the local deformation of the top faces of the specimens. During the impact, the drop hammer caused plastic indentation and crushed the concrete below. For the top steel faceplate, tensile strains were developed in the radial direction around the impact point. When the strain exceeded the ultimate strain of the steel, the faceplate would be fractured in the circumferential direction. For Specimen T03H45, a small crack exactly appeared in the faceplate near the edge of the contact region. As the impact energy increased, the drop hammer started to tear the top faceplate and penetrate the concrete, leading to more severe damage (Specimens T03H60, T03H75, and T03H75N).

The final depth (δ_{res}) and the radius (a_{res}) of the indentation zone were measured after impact and presented in Table 2. It shows that the local damage is hardly affected by the axial preload. However, from a comparison between Specimens T03H45 and T03H45N, it shows that the specimen with compressive preload was less prone to cracking under the same impact energy because a part of the tensile stress in the faceplate was counteracted by the axial compressive stress.

Table 2 Test configurations and results

Specimen	t_s /mm	H /m	V_0 /m·s ⁻¹	E_0 /kJ	N /kN	Damage description	δ_{res} /mm	a_{res} /mm	F_{mem} /kN	w_{max} /mm	w_{res} /mm	y_{max} /mm
T03H15	2.90	1.5	5.42	3.83	0	No crack	13.1	54	172	20.3	14.2	23.0
T03H30	2.90	3.0	7.67	7.67	0	No crack	24.3	75	250	32.0	24.3	36.8
T03H45	2.90	4.5	9.39	11.50	0	Just crack	33.7	90	282	41.4	32.0	50.2
T03H60	2.90	6.0	10.84	15.33	0	Tearing	46.1	105	296	47.6	36.6	64.3
T03H75	2.90	7.5	12.12	19.17	0	Tearing	64.8	115	289	53.1	43.5	85.5
T03H15N	2.90	1.5	5.42	3.83	197	No crack	12.8	52	208	19.1	13.4	21.3
T03H45N	2.90	4.5	9.39	11.50	197	No crack	33.5	90	277	37.6	29.3	50.2
T03H75N	2.90	7.5	12.12	19.17	197	Tearing	69.0	117	247	52.7	40.4	89.7
T04H45	3.80	4.5	9.39	11.50	0	No crack	13.9	75	300	36.5	18.4	45.4
T05H45	5.35	4.5	9.39	11.50	0	No crack	20.6	80	324	34.6	26.1	40.0

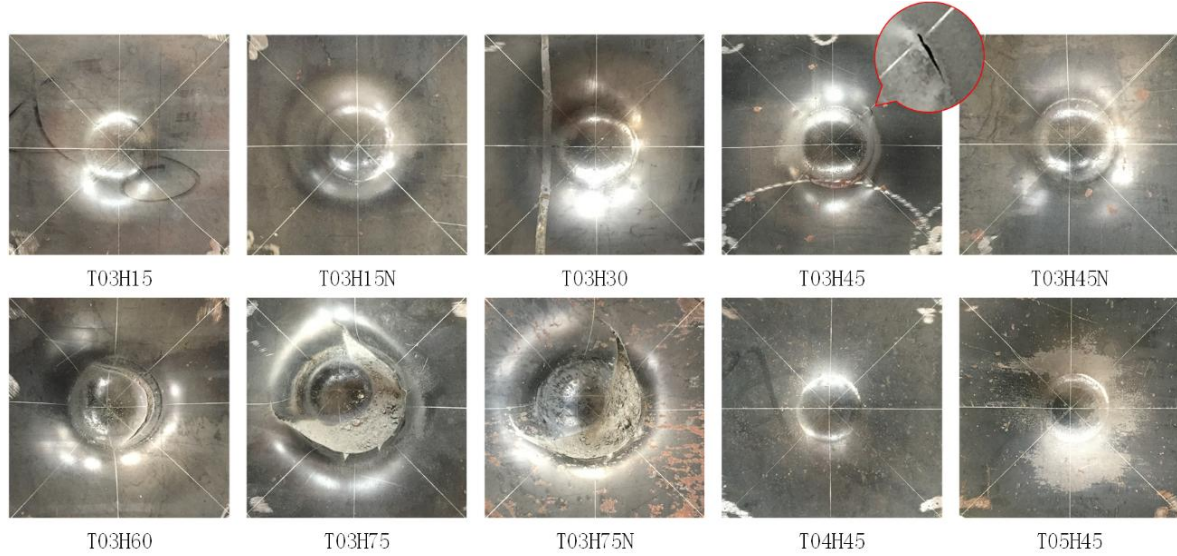


Fig. 5 Local deformations of the top steel faceplates

The local damage reduced as the thickness of the steel faceplate increased. It is noted that the indentation of Specimen T04H45 was the smallest. This could be attributed to the steel faceplate with 3.80 mm thickness which had a strength far greater than those of the others.

3.2 Time history curves

The time history curves of the impact force (F), central deflection of the bottom faceplate (w), and displacement of the drop hammer (y) are plotted in Fig. 6. The impact force acting on the interface between the drop hammer and the panel can be derived from the measured force (P) by Eq. (1), where m is the total mass of the drop hammer, and m_1 is the mass above the load cell (Holmen *et al.* 2017). With the experimental set-up in this paper the ratio of m/m_1 is about 1.03. Consequently, the impact force is slightly higher than the measured force. The acceleration derived from the impact force, hammer mass, and local gravitational acceleration are used to calculate the velocity and displacement of the drop hammer, as shown in Eq. (2) and (3). It is noted that the calculated displacement is consistent with the value captured by the high-speed camera.

$$F(t) = \frac{m}{m_1} P(t) \quad (1)$$

$$V(t) = V_0 - \int_0^t \left(\frac{F(t)}{m} - g \right) dt \quad (2)$$

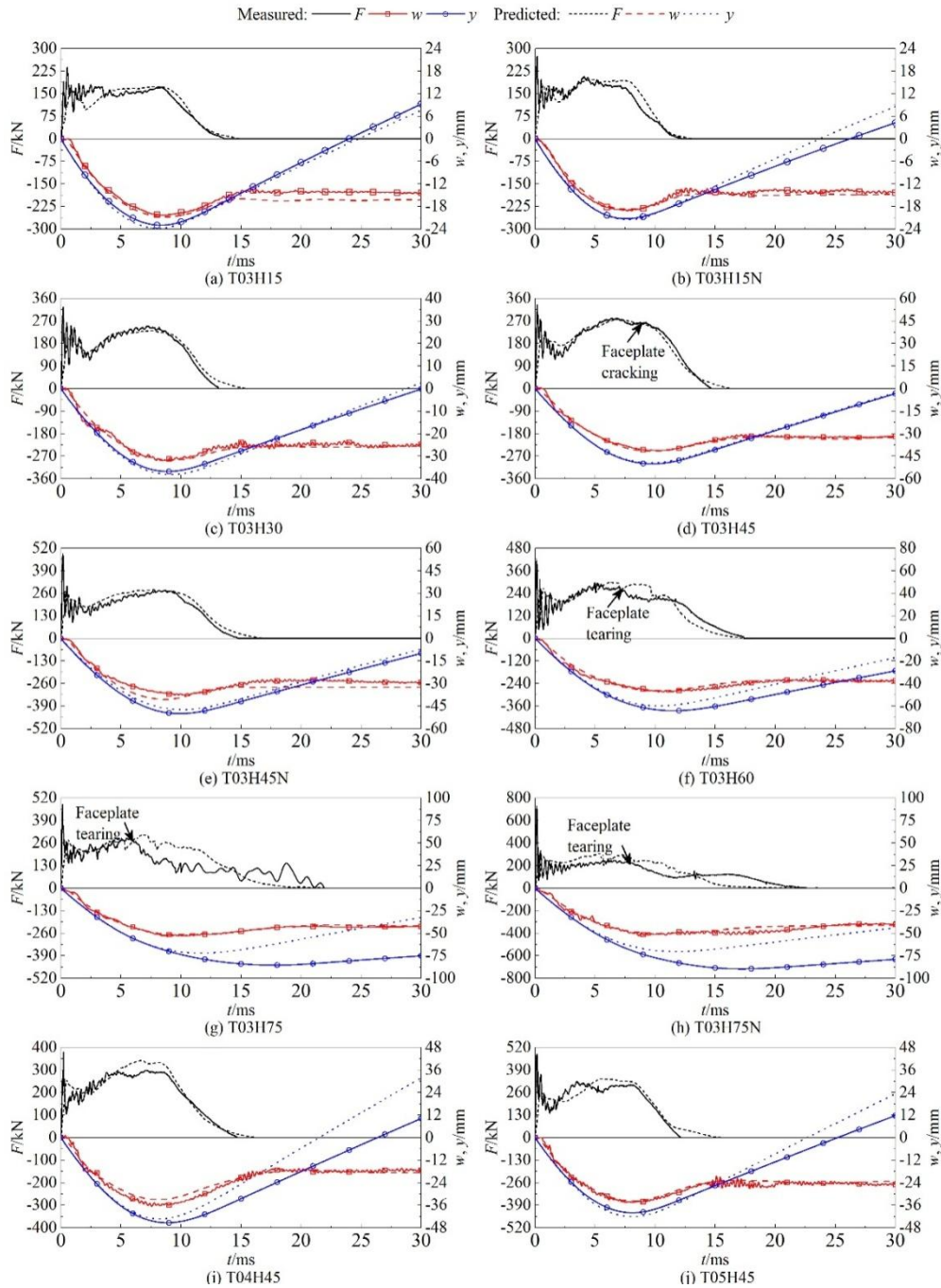
$$y(t) = \int_0^t V(t) dt \quad (3)$$

From the impact histories, it can be found that the impact force contained two peaks. The first peak was caused by the inertial effect. As the drop hammer struck the panel, a part of the measured contact force was used to accelerate the panel from rest. Therefore, the measured force could not represent the true load acting on the panel.

The second peak (F_{mem}) was caused by the membrane resistance of the panel developed at large deformation. Liew *et al.* (2009) conducted impact tests on simply supported SC beams. After the inertial response, the impact force history underwent a yielding plateau or a gradual decline caused by impact damage. The one-way SC panel tested by Remennikov *et al.* (2013) exhibited membrane resistance because axial constraints were provided. For deformed plates with non-zero Gaussian curvature, however, the membrane effects always exist at large deformation regardless of the boundary conditions (Jones 1989). For the specimens subjected to different impact energies in Series T03, the maximum membrane peak was about 290 kN (Table 2). When the drop height is greater than 4.5 m, the top steel faceplate began to crack as shown in Fig. 5. The loss of the bearing capacity of the steel faceplate also explains the decline in the impact force history curves as shown in Fig. 6. This value represents the ultimate membrane capacity of the panel and provides reference for anti-impact design.

The deformation processes of all specimens were similar. In the first few tenths of a millisecond, the deflection kept close to zero while the inertial peak had already arisen. After the overall motion was established, the panel started to bend and the deflection increased from zero to the maximum value (w_{max}). The impact energy was transformed into the elastic and plastic deformation energies of the panel. As the elastic energy stored in the panel began to release, the deflection decreased. Free vibrations were followed until the deformation went stable to a residual value (w_{res}). It is noted that the displacements of the bottom faceplate and the drop hammer increased with the increase of the impact energy. This is in accordance with the principle of energy conservation.

From a comparison of the panels impacted under the same energy, it can be found that the maximum and residual deformation of the preloaded specimen slightly decreased. But the effect of the compressive preload on the displacement of the drop hammer was not obvious. The inertial

Fig. 6 Impact force (F) and central displacement (w) history curves

peak of the preloaded specimen increased because the contact stiffness was enhanced as the degree of freedom in the axial direction was constrained. However, the effect of the compressive preload on the membrane resistance was not obvious.

As the thickness of the steel faceplate increased, the maximum displacements of the panel and the drop hammer decreased. However, the residual deflection of Specimen T04H45 was the smallest. It is noted that the yield strength of the steel faceplate used in Series T04 was much higher than the others. Hence, the proportion of elastic deformation was greater. In fact, a linear relationship can be found between the residual deflection w_{res} and $t_s f_y$. From a

comparison of the initial peaks of Specimens T03H45, T04H45 and T05H45, it can be found that the inertial peak was affected by the contact stiffness which varied due to the change in faceplate thickness. It is also noted that the membrane resistance increased linearly with respect to the faceplate thickness.

4. Numerical simulation

4.1 LS-DYNA modeling

A three-dimensional finite element (FE) model was established using ANSYS/LS-DYNA (Hallquist 2010).

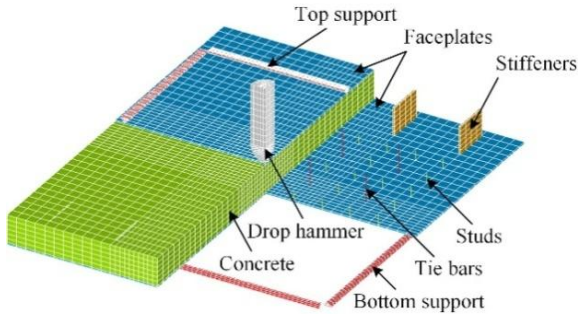


Fig. 7 A cutaway view of the finite element model

A cutaway view of the FE model is shown in Fig. 7. Solid elements (Solid164) were used for the concrete, support rollers, and the drop hammer. The steel plates were modeled using Belytschko-Tsay shell elements (Shell163). The Hughes-Liu with cross section integration beam elements (Beam161) were used to model the studs and the tie bars. From a convergence study, the mesh size was determined to be 12.5 mm near the impact point and a coarse size of 25 mm was used for other regions to save computation time without loss of accuracy. The coincident nodes of the steel faceplates and the studs/tie bars were merged in the FE model to simulate a perfect weld condition and likewise for the coincident nodes of the concrete and the connectors assuming full bond was achieved.

The translational degree-of-freedom of the nodes of the supports were restrained. As for the static axial preload, one of the loading ends was fixed with respect to the axial direction and the load was applied on the opposite end by a spring element. The stiffness of the spring (k_s) is set as 1/20 of that of the specimen, i.e., $k_s = (E_s A_s + E_c A_c) / 20$. The strain rate during the loading process was about 0.01~0.1 s^{-1} , which was in the range for a quasi-static loading. After the stress and strain went stable, the drop hammer was released using *Initial_Velocity_Generation keyword at the designed initial velocity.

The interaction between different parts in the model was defined by Automatic-Surface-to-Surface contact algorithm. The contact pairs include: (1) the supports and the steel faceplates; (2) the concrete and the steel faceplates; (3) the drop hammer with the steel faceplates and the concrete. In this study, the static and dynamic coefficients of friction applied to the interfaces between the concrete and the steel faceplates were 0.3 and 0.1, respectively. The friction between the drop hammer and the specimen was ignored. In addition, the hourglass energy was controlled using Flanagan-Belytschko with exact volume integration (type 3). A default value of 0.1 was used for the hourglass coefficient.

The material models used in this study are described as follows:

- (1) Piecewise Linear Plasticity material model (*mat_024) was specified for the steel plates and the connectors. The corresponding input parameters were obtained from the material tests as shown in Table 2. Fig. 8 shows the stress-strain curves of the steel plates. The Cowper-Symonds model was adopted to consider the strain-rate

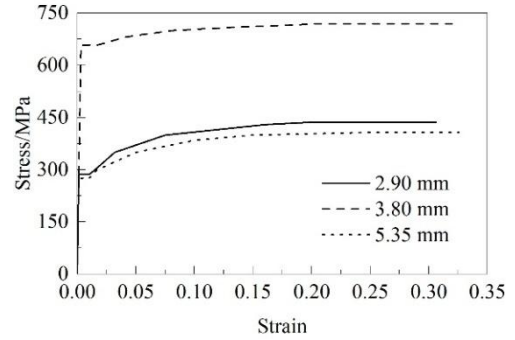


Fig. 8 Stress-strain relationship of the steel plates

effect, as shown in Eq. (4), where σ_d is the dynamic stress at a uniaxial strain rate $\dot{\epsilon}$, σ_s is the associated static stress, and coefficients D and q were set as 40.4 and 5, respectively (Jones 1989).

$$\frac{\sigma_d}{\sigma_s} = 1 + \left(\frac{\dot{\epsilon}}{D} \right)^{1/q} \quad (4)$$

- (2) The CSCM concrete model (*mat_159) was applied to the infilled concrete. This material model was frequently used in recent studies and found to be efficient in predicting the performance of structures subjected to low-velocity impact loading. The parameters can be generated automatically by providing basic material properties such as unconfined compressive strength, density, and aggregate size. Unexpected deformation due to high hourglass energy would occur when the strain-rate effect was considered. Therefore, the strain-rate effect was ignored in this study. The erosion strain (maximum principle strain) for concrete was set to be 0.35.
- (3) For the support and the drop hammer, the rigid material model (*mat_020) was used because there were only elastic deformations during impact. The mechanical properties of mild steel were assigned (Young's modulus 2.06×10^5 MPa and Poisson's ratio 0.3). Since the drop hammer in the model was simplified as a short indenter, an equivalent density was used to ensure the mass was consistent with reality.

4.2 Comparison between calculated and experimental results

The FE model predicted the local and overall deformations of the panel. The vertical displacement contour plot at the maximum deformation for Specimen T03H15, T03H45, and T03H75 are shown in Fig. 9. For the panel subjected to large impact energy, the fracture of the top steel faceplate was well simulated. The elements around the impact point were eroded due to large strain. It also shows that the damage of the concrete core was concentrated at the impact zone and the supports.

The impact force histories and displacement histories predicted by the numerical analyses are compared with the

experimental results as shown in Fig. 6. It shows that the FE model has the capacity to simulate the contact and separation phenomena during the initial stage. However, the model could not predict the exact value of the inertial peak and the high-frequency oscillations. This could be attributed to a relatively low data output frequency of 20 kHz for the purpose of saving storage space. In this study, it would not be further discussed because the inertial force does not represent the true load acting on the panel.

The FE model was able to predict the development of the membrane resistance of the panels. The displacements of the panel and the drop hammer were also well predicted. The membrane peak, the maximum and residual central deflections of the panel, and the maximum displacement of the drop hammer are compared to the experimental results in Table 3. For the panels under the largest impact energy, the model could not predict the significant drop in the

membrane resistance very well, despite the erosion of the faceplate and concrete elements. As a result, the prediction of the displacements was not very accurate, either. This could be attributed to the relatively high erosion strains of the concrete and the steel faceplates defined in the model. However, reductions of the erosion strains would lead to early penetration or even perforation. The values used in this paper were quite appropriate through the validation of the failure modes and history curves. The model overestimated the membrane resistance under the largest impact energy with a maximum difference of 26%, and the displacement of the drop hammer was underestimated with a maximum difference of 22%. For other specimens, the average difference between the measured and predicted values was within 5%.

4.3 Limit value of the axial compression ratio

The effect of the axial compressive preload was reasonably evaluated in the numerical analyses. Table 3 shows that the maximum and residual deflection of the panel decreased under the effect of axial preload. This was in accordance with the experimental results. Similar results were also found in the impact tests of prestressed concrete slabs (Kumar *et al.* 2017). However, no clear trends of the drop hammer displacement and the membrane resistance were found in the experiment since accidental errors may occur. For instance, the initial imperfection of the panel may result in different impact force histories and further affect the calculation of the drop hammer displacement. Such errors could be avoided in finite element analyses. The results showed that the drop hammer displacement decreased and the membrane resistance increased under the effect of axial preload. These changes reflected the enhancement of energy absorption of the panel.

Experimental and numerical results showed that the impact resistance of the SC panel can be improved by the axial compression at a low level. Based on the FE model developed in this paper, a parametric study was carried out to further investigate the effect of the axial preload. For the panels subjected to different impact energies in Series T03, the axial preloads were applied quasi-statically to prior to

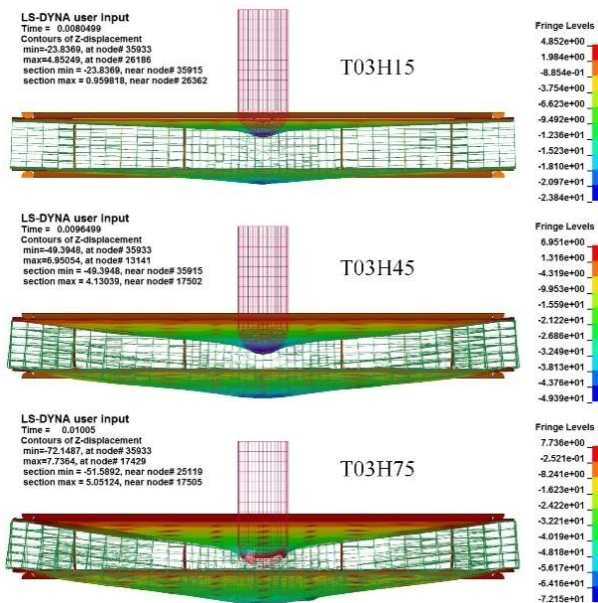


Fig. 9 Vertical displacement contour plot of the FE model at the maximum deformation

Table 3 A comparison between FE and test results

Specimen	F_{mem}/kN			w_{max}/mm			w_{res}/mm			y_{max}/mm		
	Test	FE	FE/Test	Test	FE	FE/Test	Test	FE	FE/Test	Test	FE	FE/Test
T03H15	180	173	0.961	20.3	20.8	1.025	14.4	16.3	1.132	23.0	23.8	1.035
T03H30	250	231	0.924	32.0	31.8	0.994	24.3	25.7	1.058	36.8	38.1	1.035
T03H45	282	277	0.982	41.4	41.7	1.007	32.0	32.9	1.028	50.2	49.4	0.984
T03H60	296	299	1.010	47.6	46.5	0.977	36.6	37.6	1.027	64.3	59.9	0.932
T03H75	289	310	1.073	53.1	51.5	0.970	43.5	41.3	0.949	85.5	72.1	0.843
T03H15N	208	197	0.947	19.1	18.8	0.984	13.4	14.6	1.090	21.3	21.5	1.009
T03H45N	277	279	1.007	37.6	40.8	1.085	29.3	32.5	1.109	50.2	47.7	0.950
T03H75N	247	311	1.259	52.7	50.6	0.960	40.4	41.1	1.017	89.7	70.3	0.784
T04H45	300	333	1.110	36.5	32.9	0.901	18.4	17.3	0.940	45.4	43.3	0.954
T05H45	324	340	1.049	34.6	33.8	0.977	26.1	24.3	0.931	40.0	42.1	1.053
Average	-	-	1.032	-	-	0.988	-	-	1.028	-	-	0.958

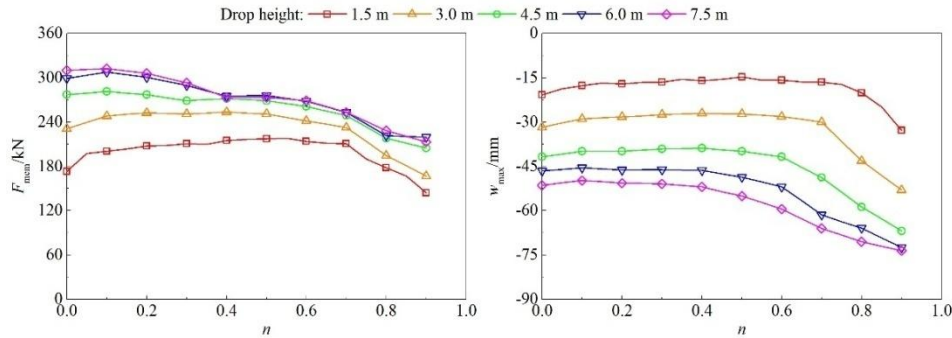


Fig. 10 Membrane peak (F_{mem}) and maximum displacement (w_{max}) versus axial compression ratio (n) curves

impact at axial compression ratios ranging from 0 to 0.9. The membrane peaks (F_{mem}) and the maximum central displacements (w_{max}) versus axial compression ratio curves are given in Fig. 10.

For the specimens under the lowest impact energy ($H = 1.5$ m), Fig. 10 shows that: when the axial compression ratio is less than 0.8, the membrane peak of the panel increases by up to 26%, and the central displacement decreases by 29%; when the axial compression ratio is greater than 0.8, the impact resistance of the panel significantly reduced.

Test results showed that the specimen reached a maximum resistance of 290 kN when the drop height was greater than 4.5 m. In Fig. 10, it is noted that the membrane peaks for 6 m and 7.5 m drop height cases are quite close because the maximum resistance is reached. These $F_{mem}-n$ curves can be taken as the envelop curve. The impact force cannot exceed the envelop curve because the top steel plate fails and loses bearing capacity.

Under the action of the axial preload and the impact loading, the bearing mechanism of the panel along the plastic hinge line is similar with that of a column under eccentric compression. Therefore, a critical axial compression ratio exists. When the axial compression ratio is greater than the critical value, the impact resistance of the panel significantly reduced, and vice visa.

As the axial compression increases, the envelop curve declines. When the axial compression ratio is smaller than 0.4, the resistance is controlled by the membrane capacity of the specimen. Fig. 10 shows that the resistance increases with the increase of the drop height until it reaches 6 m. When the axial compression ratio is greater than 0.4, the resistance is controlled by the failure of the steel plate. The resistance cannot get higher when the drop height increases to 4.5 m.

Fig. 10 shows that with the increase of the impact energy, the enhancement of the impact resistance caused by the axial preload weakens, and the critical axial compression ratio decreases from 0.8 to 0.3. To consider the worst situation under extreme impact loadings, it is suggested that the axial compression ratio does not exceed 0.3.

5. Conclusions

Instrumented drop hammer impact tests and numerical

simulation were conducted on SC panels. The parameters studied in this paper included the impact energy, thickness of the steel faceplate, and axial compressive preload. Based on the results presented in this paper, the following conclusions were drawn:

- (1) The deformation of SC panels under impact consists of local indentation and overall bending. As the top steel faceplate started to fail, the resistance would significantly decrease. The failure mode was dominated by local punching.
- (2) A three-dimensional FE model was established in LS-DYNA to predict the impact response of SC panels, in which the effect of axial preload was reasonably considered. From the comparison of the numerical and experimental results, it can be concluded that the FE model is capable of describing the most important structural characteristics of SC panels under low-velocity impact.
- (3) The effect of axial compressive preload at a low level could be beneficial to the impact response, which is reflected by the enhancement of the impact force and the reduction of deformation. However, when the axial compression ratio exceeds a certain value, the impact resistance significantly reduces. The critical axial compression ratio is suggested to be 0.3.

Acknowledgments

This work was financially supported by National Natural Science Foundation of China (Grant No. 51578032). The support is gratefully acknowledged.

References

- ANSI/AISC N690s1-15 (2015), Specification for Safety-Related Steel Structures for Nuclear Facilities, American Institute of Steel Construction; Chicago, IL, USA.
- Barr, P. (1990), Guidelines for the design and assessment of concrete structures subjected to impact; Safety and Reliability Directorate.
- Bruhl, J., Johnson, W.H., Reigles, D.G., Li, J., Varma, A.H. and Kim, J.M. (2015a), "Impact assessment of SC walls using idealized SDOF and TDOF models", *ASCE Structures Congress*, Portland, OR, USA.

- Bruhl, J.C., Varma, A.H. and Kim, J.M. (2015b), "Static resistance function for steel-plate composite (SC) walls subject to impactive loading", *Nucl. Eng. Des.*, **295**, 843-859.
- Grisaro, H. and Dancygier, A.N. (2014), "Assessment of the perforation limit of a composite RC barrier with a rear steel liner to impact of a non-deforming projectile", *Int. J. Impact Eng.*, **64**(2), 122-136.
- Grisaro, H. and Dancygier, A.N. (2015), "Assessment of residual deformation of rear steel plate in RC barriers subjected to impact of non-deforming projectiles", *Int. J. Impact Eng.*, **77**, 42-58.
- Hallquist, J.O. (2010), *LS-DYNA keyword user's manual*, vol. 1, Version 971, Livermore Software Technology Corporation (LSTC).
- Hashimoto, J., Takiguchi, K., Nishimura, K., Matsuzawa, K., Tsutsui, M., Ohashi, Y., Kojima, I. and Torita, H. (2005), "Experimental study on behavior of RC panels covered with steel plates subjected to missile impact", *Proceedings of the 18th International Conference on Structural Mechanics in Reactor Technology (SMiRT 18)*, Beijing, China, August.
- Holmen, J.K., Olovsson, L. and Børvik, T. (2017), "Discrete modeling of low-velocity penetration in sand", *Comput. Geotech.*, **86**, 21-32.
- JEAC 4618-2009 (2009), Technical code for seismic design of steel plate reinforced concrete structures: Buildings and structures, Japan Electric Association Nuclear Standards Committee; Tokyo, Japan.
- Jones, N. (1989), *Structural Impact*, Cambridge University Press
- Kennedy, R.P. (1975), "A review of procedures for the analysis and design of concrete structures to resist missile impact effects", *Nucl. Eng. Des.*, **37**(2), 183-203.
- KEPIC-SNG (2010), Specification for safety-related steel plate concrete structures for nuclear facilities; Korea Electric Association.
- Kong, S.Y., Remennikov, A.M. and Uy, B. (2013), "An experimental investigation of the performance of non-composite steel-concrete-steel protective panels under large impact loading", *Adv. Struct. Eng.*, **16**(7), 1163-1174.
- Kumar, V., Iqbal, M.A. and Mittal, A.K. (2017), "Behaviour of prestressed concrete under drop impact loading", *Procedia Engineering*, **173**, 403-408.
- Lee, H.K. and Kim, S.E. (2016), "Comparative assessment of impact resistance of SC and RC panels using finite element analysis", *Prog. Nuclear Energy*, **90**, 105-121.
- Liew, J.Y.R., Sohel, K.M.A. and Koh, C.G. (2009), "Impact tests on steel-concrete-steel sandwich beams with lightweight concrete core", *Eng. Struct.*, **31**(9), 2045-2059.
- Mizuno, J., Koshika, N., Sawamoto, Y., Niwa, N., Yamashita, T. and Susuki, A. (2005), "Investigation on impact resistance of steel plate reinforced concrete barriers against aircraft impact Part 1: Test program and results", *Proceedings of the 18th International Conference on Structural Mechanics in Reactor Technology (SMiRT 18)*, Beijing, China, Month.
- Remennikov, A.M. and Kong, S.Y. (2012), "Numerical simulation and validation of impact response of axially-restrained steel-concrete-steel sandwich panels", *Compos. Struct.*, **94**(12), 3546-3555.
- Remennikov, A.M., Kong, S.Y. and Uy, B. (2013), "The response of axially restrained non-composite steel-concrete-steel sandwich panels due to large impact loading", *Eng. Struct.*, **49**, 806-818.
- Sadiq, M., Xiuyun, Z. and Rong, P. (2014), "Simulation analysis of impact tests of steel plate reinforced concrete and reinforced concrete slabs against aircraft impact and its validation with experimental results", *Nucl. Eng. Des.*, **273**, 653-667.
- Sliter, G.E. (1980), "Assessment of empirical concrete impact formulas", *J. Struct. Div.*, **106**(5), 1023-1045.
- Sohel, K.M.A. and Liew, J.Y.R. (2014), "Behavior of steel-concrete-steel sandwich slabs subject to impact load", *J. Constr. Steel Res.*, **100**, 163-175.
- Tsubota, H., Kasai, Y., Koshika, N., Morikawa, H., Uchida, T., Ohno, T. and Kogure, K. (1993), "Quantitative studies on impact resistance of reinforced concrete panels with steel liners under impact loading. Part 1: Scaled model impact tests", *Proceedings of the 12th International Conference on Structural Mechanics in Reactor Technology (SMiRT 12)*, Stuttgart, Germany, August.
- Walter, T.A. and Wolde-Tinsae, A.M. (1984), "Turbine missile perforation of reinforced concrete", *J. Struct. Eng.*, **110**(10), 2439-2455.
- Wang, R., Han, L.H. and Hou, C.C. (2013), "Behavior of concrete filled steel tubular (CFST) members under lateral impact: Experiment and FEA model", *J. Constr. Steel Res.*, **80**(1), 188-201.

BU